ATLAS NOTE

ATLAS-CONF-2013-093

August 27, 2013

Search for chargino and neutralino production in final states with one lepton, two b-jets consistent with a Higgs boson, and missing transverse momentum with the ATLAS detector in 20.3 fb^{-1} of $\sqrt{s}$ = 8 TeV pp collisions

The ATLAS Collaboration

Abstract

A search for direct production of charginos ($\tilde{\chi}_1^{\pm}$) and neutralinos ($\tilde{\chi}_2^0$) in final states with one charged lepton (electron or muon), missing transverse momentum, and two jets identified as originating from b-quarks and consistent with a 125 GeV Higgs boson is performed. The analysis uses 20.3 fb^{-1} of proton–proton collision data at $\sqrt{s}$ = 8 TeV recorded in 2012 with the ATLAS detector at the Large Hadron Collider. No excess is observed with respect to the expectations from Standard Model processes. The results are interpreted in the context of simplified supersymmetric models considering $pp \to \tilde{\chi}_1^{\pm}\tilde{\chi}_2^0$ production followed by $\tilde{\chi}_1^{\pm} \to W^{\pm}(\to \ell^{\pm}\nu)\tilde{\chi}_1^0$ and $\tilde{\chi}_2^0 \to h(\to b\bar{b})\tilde{\chi}_1^0$, where $\tilde{\chi}_1^0$ is the lightest neutralino and supersymmetric particle and $m_{\tilde{\chi}_1^{\pm}} = m_{\tilde{\chi}_2^0}$ is assumed. For a massless $\tilde{\chi}_1^0$, mass ranges of $125 < m_{\tilde{\chi}_1^{\pm},\tilde{\chi}_2^0} < 141$ GeV and $166 < m_{\tilde{\chi}_1^{\pm},\tilde{\chi}_2^0} < 287$ GeV are excluded at 95% confidence level, determined at -1σ signal theoretical uncertainty, for an expected exclusion range of $225 < m_{\tilde{\chi}_1^{\pm},\tilde{\chi}_2^0} < 235$ GeV.

ATLAS-CONF-2013-093
28 August 2013

1 Introduction

Supersymmetry (SUSY) [1–9] is an extension to the Standard Model (SM), which relates fermions and bosons. For every known boson (fermion) of the SM, it postulates the existence of a yet unseen fermionic (bosonic) partner. The introduction of these new particles provides solutions to the hierarchy problem [10–13]. Under the assumption that R-parity is conserved [14–18], a dark matter candidate is also provided in the form of the lightest supersymmetric particle (LSP). R-parity conserving scenarios are considered in this note, hence SUSY particles are always produced in pairs.

Gluinos ($\tilde{g}$) and squarks ($\tilde{q}$) are the SUSY partners of gluons and quarks. Sleptons are the SUSY partners of the SM leptons. Charginos ($\tilde{\chi}_i^{\pm}$ with i=1,2) and neutralinos ($\tilde{\chi}_j^0$ with j=1,2,3,4) are the mass eigenstates formed from the linear superpositions of the SUSY partners of the Higgs and electroweak gauge bosons. The lightest neutralino ($\tilde{\chi}_1^0$) is often considered to be the LSP. Naturalness arguments [19, 20] suggest that the charginos and neutralinos have masses in the hundreds of GeV range. Their direct production may be the dominant SUSY production mode at the LHC under the hypothesis that the masses of gluinos and squarks are greater than a few TeV.

This note presents a search targeting the process shown in Figure 1, in which direct production of a chargino-neutralino pair $pp \to \tilde{\chi}_1^{\pm}\tilde{\chi}_2^0$ is followed by the chargino decay $\tilde{\chi}_1^{\pm} \to W^{\pm}(\to \ell^{\pm}\nu)\tilde{\chi}_1^0$ and the neutralino decay $\tilde{\chi}_2^0 \to h(\to b\bar{b})\tilde{\chi}_1^0$, where the $\tilde{\chi}_1^0$ is the LSP and $\tilde{\chi}_1^{\pm}$ and $\tilde{\chi}_2^0$ are assumed to be mass degenerate. The targeted final-state signature contains one lepton (electron or muon), two jets identified as originating from b-quarks (b-jets) consistent with a Higgs boson, and large missing transverse momentum due to the neutrino and the two neutralinos in the decay, which is inspired from the equivalent SM search for associated W/Z+H production [21]. Both the ATLAS and CMS collaborations have performed searches [22–25] for the production of $\tilde{\chi}_1^{\pm}$-$\tilde{\chi}_2^0$ through various decay modes. The search presented here focuses on a complimentary scenario exploiting the presence of a Higgs boson in the decay chain, and is performed for the first time at the LHC.

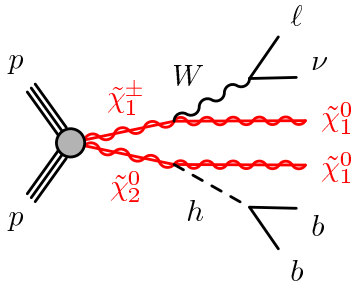

Figure 1: The chargino-neutralino production process targeted in this search.

2 The ATLAS Detector

The ATLAS experiment [26] is a multi-purpose particle physics detector located at the LHC at CERN. Its cylindrical geometry nearly covers 4π in solid angle. The magnetic field is provided by two magnet systems: a solenoid produces a 2 Tesla magnetic field around the inner tracking detector (ID). Outside the calorimeters, but within the muon system, a toroidal magnetic field is produced by superconducting barrel loops and end-cap toroidal magnets. The ID covers the pseudorapidity[1] region $|\eta| < 2.5$ and

[1]ATLAS uses a right-handed coordinate system with its origin at the nominal interaction point (IP) in the centre of the detector and the z-axis coinciding with the axis of the beam pipe. The x-axis points from the IP to the centre of the LHC ring, and the y-axis points upward. Cylindrical coordinates (r,ϕ) are used in the transverse plane, ϕ being the azimuthal angle around

consists of a silicon pixel detector, a silicon microstrip detector (SCT), and a transition radiation tracker (TRT). The calorimeter consists of two systems. A high-granularity inner electromagnetic calorimeter (EM) using liquid argon as active detector medium covers the pseudorapidity region $|\eta| < 3.2$. The electromagnetic coverage at higher pseudorapidity $3.1 < |\eta| < 4.9$ is provided by the forward calorimeter (FCal), a copper-tungsten/liquid-argon detector. An outer iron-scintillator hadronic calorimeter provides coverage for hadron detection for the pseudorapidity region $|\eta| < 1.7$. The detection of hadrons at higher pseudorapidity $1.5 < |\eta| < 4.9$ is provided by the hadronic end-cap calorimeter, a copper/liquid-argon detector, and the FCal. The muon spectrometer surrounds the calorimeters and consists of a system of precision tracking chambers ($|\eta| < 2.7$), and detectors for triggering ($|\eta| < 2.4$).

3 Data Samples

3.1 Experimental Data

The data used in this analysis were collected by the ATLAS detector during the 2012 proton-proton collision runs at $\sqrt{s} = 8$ TeV. They represent a total integrated luminosity of $20.3\,\text{fb}^{-1}$ after applying beam, detector and data-quality requirements.

Events are triggered using a combination of single-electron and single-muon triggers. To control the trigger rates, isolation requirements are defined at the trigger level by applying a cut on the maximal energy found in cones centered on the lepton direction. Isolated-lepton triggers with lower p_{T} thresholds are combined with higher-p_{T} lepton triggers without isolation requirements. For the electron trigger, the p_{T} thresholds are 24 GeV (isolated) and 60 GeV (non-isolated). For the muon trigger, the corresponding p_{T} thresholds are 24 GeV and 36 GeV, respectively.

3.2 Simulated Data

Monte Carlo (MC) simulated event samples are used to evaluate SM backgrounds in the signal regions, and to assess the sensitivity to potential SUSY signals. They are produced using simulation based either solely on `GEANT4` [27] or on a combination of `GEANT4` and fast calorimeter simulation [28,29]. The effect of multiple proton-proton collisions (pile-up) from the same or different bunch crossings is incorporated into the simulation by overlaying additional minimum bias events onto hard-scatter events. Simulated events are weighted to match the distribution of the number of interactions per bunch crossing observed in data.

3.2.1 Standard Model Backgrounds

Dominant sources of SM background include top quarks ($t\bar{t}$ or single top) and W bosons produced in association with hadronic jets.

The production of top quark pairs is simulated with `POWHEG-BOX` r2129 [30], with hadronisation performed with `PYTHIA` 6.426 [31], using a top quark mass of 172.5 GeV. Additional samples generated with `MC@NLO` 4.06 [32, 33] and `ACERMC` 3.8 [34] are used for cross checks and to estimate systematic uncertainties. The $t\bar{t}$ cross section is calculated at approximately the next-to-next-to-leading order (NNLO) [35, 36]. Single top production is modelled with `POWHEG-BOX` for the Wt mode and s-channel, and with `ACERMC` for the t-channel using a diagram reduction scheme for $t\bar{t}$ interference [37]. Additional single-top samples used for systematic uncertainties at particle level are generated with `MC@NLO` and `ACERMC`. Alternative $t\bar{t}$ and single top samples generated with `POWHEG-BOX` interfaced to

the beam pipe. The pseudorapidity is defined in terms of the polar angle θ as η = - ln tan(θ/2).

HERWIG 6.520 [38] and JIMMY 4.31 [39] are used for the evaluation of systematic uncertainties on the modeling of the parton shower.

Samples of $W \to \ell\nu$ and $Z/\gamma^* \to \ell\ell$ produced in association with light and heavy flavour jets are generated with SHERPA 1.4.1 [40] which treats b and c quarks as massive. Additional samples are generated with ALPGEN 2.6 [41] for theory systematic uncertainties. The theoretical cross sections for W and Z/γ^* are calculated at NNLO accuracy using DYNNLO [42,43] with the MSTW2008NNLO [44] PDF set.

Diboson (WW, WZ and ZZ) production is simulated with HERWIG. Additional samples are generated with SHERPA to estimate systematic uncertainties on the diboson modeling. The diboson cross sections are calculated using NLO QCD predictions obtained with MCFM [45, 46]. The production of $t\bar{t}$ associated with a vector boson is simulated with MADGRAPH5 v1.3.33 [47] and scaled to the NLO cross section [48,49]. The production of the Higgs boson in association with W and Z (WH and ZH) is generated with PYTHIA 8.165 and 8.163. The WH and ZH samples are normalised to the NLO cross sections as calculated in Ref. [50].

Fragmentation and hadronisation for the MC@NLO and POWHEG-BOX samples are performed either with HERWIG, or with PYTHIA. PYTHIA is used for the ACERMC, ALPGEN and MADGRAPH5 samples.

3.2.2 SUSY Signal

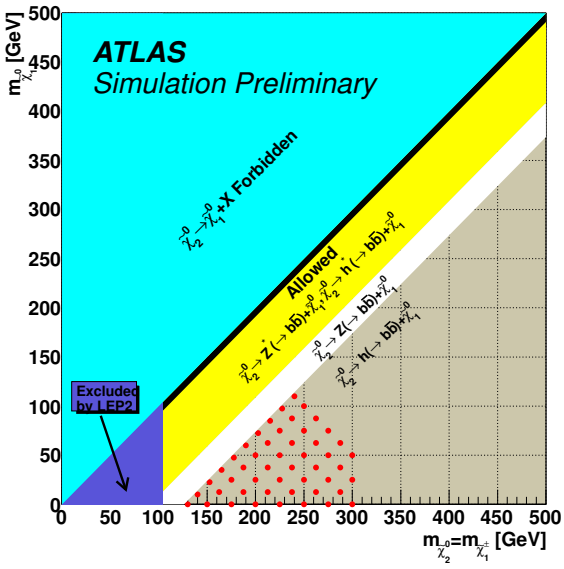

Figure 2: Illustration of the SUSY signal models considered in this search as a function of the $\tilde{\chi}_1^{\pm}/\tilde{\chi}_2^0$ and $\tilde{\chi}_1^0$ masses. The areas below the black diagonal line are the regions where the following decays are dominant: $\tilde{\chi}_2^0$ decays to a virtual Z or Higgs boson and $\tilde{\chi}_1^0$ (yellow), $\tilde{\chi}_2^0$ decays to a real Z boson and $\tilde{\chi}_1^0$ (white) and $\tilde{\chi}_2^0$ decays to a real Higgs boson and $\tilde{\chi}_1^0$ (grey). The red dots indicate the samples generated, where BR($\tilde{\chi}_2^0 \to h\,\tilde{\chi}_1^0$) = 100% is assumed.

The results of the search are interpreted in the context of simplified models where the masses and decay modes of the relevant particles ($\tilde{\chi}_1^{\pm}$, $\tilde{\chi}_2^0$, $\tilde{\chi}_1^0$) are the only free parameters, while the slepton and squark masses are assumed to be effectively decoupled. Samples are generated with HERWIG++ [51] and include associated production of $\tilde{\chi}_1^{\pm}$ and $\tilde{\chi}_2^0$, which are set to be wino-like and mass degenerate, i.e. $m_{\tilde{\chi}_1^{\pm}} = m_{\tilde{\chi}_2^0}$. The $\tilde{\chi}_1^0$ is set to be bino-like. Charginos and neutralinos are assumed to decay with 100%

branching ratio in $W^{\pm}\tilde{\chi}_1^0$ and $h\,\tilde{\chi}_1^0$, respectively.[2] The Higgs mass is set to 125 GeV and decay modes branching ratios are assumed to be the same as in the SM, with a $h \to b\bar{b}$ branching fraction of 58%.

Figure 2 shows the generated SUSY models as a function of the $\tilde{\chi}_1^{\pm}/\tilde{\chi}_2^0$ and $\tilde{\chi}_1^0$ masses. The $m_{\tilde{\chi}_1^{\pm},\tilde{\chi}_2^0}$ values excluded by LEP are also shown. Samples are produced with $m_{\tilde{\chi}_1^{\pm}} = m_{\tilde{\chi}_2^0}$ between 130 GeV and 300 GeV and assuming $\Delta m = (m_{\tilde{\chi}_1^{\pm},\tilde{\chi}_2^0} - m_{\tilde{\chi}_1^0})$ above 130 GeV to allow on-shell decays of $\tilde{\chi}_2^0$ via a Higgs boson.

Signal cross sections are calculated to NLO accuracy using PROSPINO2 [52] under the hypothesis described above. As an example, for $m_{\tilde{\chi}_1^{\pm}} = m_{\tilde{\chi}_2^0} = 130$ GeV, the production cross section is 4.2 pb and it decreases to 0.15 pb at 300 GeV.

4 Event Selection

The vertex candidates for the pp interactions in each event are reconstructed from the ID tracks. The primary vertex, corresponding to the hard scattering interaction, is the vertex candidate with the largest sum of p_{T}^2 for the associated tracks. Events with at least five charged tracks associated to the primary vertex are selected. In each event, candidate electrons, muons, and jets are reconstructed. After removing potential overlaps between these objects, criteria to define signal electrons, muons, and jets are refined.

Candidate electrons are reconstructed by matching clusters in the EM calorimeter with charged tracks in the ID. They are then required to have $p_{\mathrm{T}} > 10$ GeV and $|\eta| < 2.47$. They must pass the "medium++" shower-shape and track-selection criteria defined in Ref. [53].

Candidate muons are reconstructed by matching a muon spectrometer track with an ID track. They are required to have $p_{\mathrm{T}} > 10$ GeV and $|\eta| < 2.4$ and must be reconstructed with sufficient hits in the pixel, SCT and TRT detectors to ensure a good track reconstruction [54]. Events containing muons that are likely to have arisen from beam-induced backgrounds or cosmic rays are rejected.

Candidate jets are reconstructed using the anti-k_t jet clustering algorithm [55] with a distance parameter of 0.4. The jet candidates are corrected for the effects of calorimeter non-compensation and inhomogeneities by using p_{T} and η-dependent calibration factors based on MC simulations and validated with extensive test-beam and collision-data studies [56]. They are then required to have $p_{\mathrm{T}} > 20$ GeV and $|\eta| < 4.5$. Events containing jets that are likely to have arisen from detector noise are rejected.

Object overlaps are defined in terms of $\Delta R = \sqrt{(\Delta\eta)^2 + (\Delta\phi)^2}$, where $\Delta\eta$ and $\Delta\phi$ are separations in η and ϕ between the two objects. If two electron candidates are within $\Delta R = 0.1$ of each other, only the one with the larger transverse energy E_T is considered. Jet candidates are rejected if they lie within $\Delta R = 0.2$ of any electron. Lepton candidates lying within $\Delta R = 0.4$ of any remaining jets are removed. If an electron candidate and a muon candidate lie within $\Delta R = 0.1$ of each other or two muon candidates lie within $\Delta R = 0.05$ of each other, the event is rejected.

Signal electrons must have $p_T > 25$ GeV and must be isolated: the p_{T} sum of tracks above 400 MeV within a cone of size $\Delta R = 0.3$ around the electron candidate (excluding the electron candidate itself) is required to be less than 16% of the electron p_{T}. The sum of transverse energies of the surrounding topological clusters within $\Delta R = 0.3$ of each electron candidate, corrected for deposition of energy from pile-up events, is required to be less than 18% of the electron p_{T}. The distance of closest approach of an electron candidate to the event primary vertex in the transverse plane must be less than 5 standard deviations. The distance along the beam direction, z_0, must satisfy $|z_0| \sin\theta < 0.4$ mm. In addition, signal electrons must pass the "tight++" criteria defined in Ref. [53] placed on the ratio of calorimetric energy to track momentum, and the number of high-threshold hits in the TRT.

[2] Scenarios where the wino-like $\tilde{\chi}_2^0$ decays preferentially to a bino-like $\tilde{\chi}_1^0$ and a Higgs boson as opposed to a Z boson can be realized in phenomenological minimal supersymmetric models (pMSSM). Although the former decay is suppressed by the mixing of the wino-like $\tilde{\chi}_2^0$ to higgsino, the latter decay is additionally suppressed by the mixing of the bino-like $\tilde{\chi}_1^0$ to higgsino.

Signal muons must have $p_T > 25$ GeV and be isolated: the p_{T} sum of tracks above 1 GeV within a cone of size $\Delta R = 0.3$ around the muon candidate (excluding the muon candidate itself) is required to be less than 12% of the muon p_{T}. The transverse energies of the surrounding topological clusters within $\Delta R = 0.3$ of each muon candidate, corrected for deposition of energy from pile-up events, must satisfy the same requirement. The distance of closest approach in the transverse plane of a muon candidate to the event primary vertex must be within 3 standard deviations. The distance along the beam direction must satisfy $|z_0| \sin\theta < 0.4\,\mathrm{mm}$.

Signal jets are classified in two exclusive categories. Central jets satisfy $p_{\mathrm{T}} > 25$ GeV and $|\eta| < 2.4$. If a central jet has $p_{\mathrm{T}} < 50$ GeV and has charged tracks associated to it, at least 50% of the sum of the p_{T} of the charged tracks must belong to those that are consistent with originating from the primary vertex. This reduces the pile-up side effects by suppressing pile-up jets associated to another vertex. Forward jets are those with $2.4 \leq |\eta| < 4.5$ and $p_{\mathrm{T}} > 30$ GeV.

A b-tagging algorithm [57], which exploits the long lifetime of b- and c-hadron inside a candidate jet, is used to identify b-jets. The mean nominal b-tagging efficiency, determined from $t\bar{t}$ MC events, is 70%, with a misidentification rates of 0.73% for light-quark jets and 20% for charm jets. Scale factors (which depend on p_{T}) determined from data are applied to all MC samples to correct differences between data and MC efficiencies. Only central jets ($|\eta| < 2.4$) may be b-tagged as forward jets lie outside the tracker.

The measurement of the missing transverse momentum two-vector, $\mathbf{p}_{\mathrm{T}}^{\mathrm{miss}}$, and its magnitude, $E_{\mathrm{T}}^{\mathrm{miss}}$, is based on the transverse momenta of all electron and muon candidates, all jets, and all clusters of calorimeter energy with $|\eta| < 4.9$ not associated to such objects.

At this point, events with exactly one signal lepton and two b-tagged jets are selected. Events are rejected if they contain more than one candidate lepton. The signal lepton is required to have triggered the event, and its p_{T} must be above the efficiency plateau threshold of the corresponding trigger. The b-tagged jets must be the two highest-p_{T} jets in the event, and there must not be more than one additional signal jet. The events that pass this selection, labeled preselection henceforth, are subject to further selection criteria described in the next section, which define the control, validation and signal regions of this search.

5 Signal Regions

After the preselection two non-overlapping signal regions, denoted SRA and SRB, are defined to suppress the SM background and enhance the purity of the SUSY signal. The two signal regions are optimized for SUSY signal models with large Δm between $\tilde{\chi}_1^{\pm}/\tilde{\chi}_2^0$ and $\tilde{\chi}_1^0$, and are designed to provide the best sensitivity depending on the $\tilde{\chi}_1^{\pm}/\tilde{\chi}_2^0$ mass, with SRA (SRB) being most sensitive at low (high) $\tilde{\chi}_1^{\pm}/\tilde{\chi}_2^0$ masses. The signal regions are defined in terms of four kinematic variables: $E_{\mathrm{T}}^{\mathrm{miss}}$, m_{CT}, m_{T} and m_{bb}.

Events in the signal regions must satisfy $E_{\mathrm{T}}^{\mathrm{miss}} > 100$ GeV for both SRA and SRB.

The contransverse mass, m_{CT}, was originally designed to measure the mass of pair produced heavy particles which decay identically and semi-invisibly [58, 59]. It is given without boost correction by:

$$m_{\mathrm{CT}}^2 = \left(E_{\mathrm{T}}^{b_1} + E_{\mathrm{T}}^{b_2}\right)^2 - \left|\mathbf{p}_{\mathrm{T}}^{b_1} - \mathbf{p}_{\mathrm{T}}^{b_2}\right|^2, \tag{1}$$

where b_1 and b_2 are the two b-jets. In the case where b_1 and b_2 are essentially massless, this formula reduces to:

$$m_{\mathrm{CT}}^2 \approx 2 p_{\mathrm{T}}^{b_1} p_{\mathrm{T}}^{b_2} (1 + \cos\Delta\phi_{bb}). \tag{2}$$

A useful feature of the m_{CT} is that it has a kinematic endpoint given (in the limit of the visible particle

being massless) by:

$$m_{\mathrm{CT}}^{\mathrm{max}} \approx \frac{m_{\mathrm{heavy}}^2 - m_{\mathrm{invisible}}^2}{m_{\mathrm{heavy}}} \tag{3}$$

Backgrounds from $t\bar{t}$ events with large $E_{\mathrm{T}}^{\mathrm{miss}}$ are primarily due to dileptonic decays where one of the two leptons is not identified, is outside the detector acceptance or is a hadronically decaying tau lepton. Since m_{CT} depends only on the kinematics of the two b-jets, it is effective in removing such events. For both SRA and SRB, $m_{\mathrm{CT}} > 160$ GeV is required.

To help remove the W background, the transverse mass m_{T} , defined by

$$m_{\mathrm{T}} = \sqrt{2p_{\mathrm{T}}^{\mathrm{lep}} E_{\mathrm{T}}^{\mathrm{miss}} - 2\mathbf{p}_{\mathrm{T}}^{\mathrm{lep}} \cdot \mathbf{p}_{\mathrm{T}}^{\mathrm{miss}}}, \tag{4}$$

is used with the requirements $100 < m_{\mathrm{T}} < 130$ GeV for SRA and $m_{\mathrm{T}} > 130$ GeV for SRB. The distributions of these variables at preselection level are shown in Figure 3, after normalizing the SM background to data in the control regions as described in Section 6.

Finally, the invariant mass of the two b-jets, m_{bb}, is required to be larger than 50 GeV. This requirement is further refined by defining exclusive bins that are simultaneously fitted, as detailed in Section 8. The majority of signal events is expected to be found in the region around the Higgs mass value: in the following, SRAh and SRBh refer to SRA and SRB with the additional requirement $105 < m_{bb} < 135$ GeV.

The definitions of the signal regions are summarized in Table 1, together with the control and validation regions discussed in Section 6.

MC-based estimates indicate that for SRA (SRB), 47% (31%) of the SM background is constituted by $t\bar{t}$ events and 27% (20%) by events from W+jets production, where jets are mostly b-jets. Additional contributions arise from single top (21% and 36% for SRA and SRB, respectively), diboson, Z+jets, $t\bar{t}$+V and SM Higgs production (where the summed contribution is 5% and 12% for SRA and SRB, respectively).

The sensitivity of this search is limited at larger $m_{\tilde{\chi}_1^\pm,\tilde{\chi}_2^0}$ by the rapidly falling production cross section, as well as by the low acceptance. Within the simplified-model framework with a bino-like $\tilde{\chi}_1^0$ and a wino-like $\tilde{\chi}_1^\pm$, the expected signal yield is 8.7 (0.4) events in SRA (SRB) for $(m_{\tilde{\chi}_1^\pm,\tilde{\chi}_2^0}, m_{\tilde{\chi}_1^0}) = (130, 0)$ GeV, and 2.5 (5.7) events in SRA (SRB) for $(m_{\tilde{\chi}_1^\pm,\tilde{\chi}_2^0}, m_{\tilde{\chi}_1^0}) = (225, 0)$ GeV while the product of acceptance and efficiency ranges from 0.1% (0.05%), at low Δm, to 0.3% (1.2%), at large Δm, for SRA (SRB).

6 Control and Validation Regions

As discussed in Section 5, the main SM background contributions in the signal regions arise from $t\bar{t}$, single-top and W + jets production. For $t\bar{t}$ and W + jets (mostly b-jets), two background-enriched control regions (CR1 and CR2) are defined, and their event yields are used to normalise the predicted background contributions in the SRs. The control regions are defined such that they are as close as possible kinematically to the signal regions to minimize extrapolation effects while keeping a low signal contamination. Single top and other sources of irreducible background are estimated with MC simulation. Background events in which the signal lepton did not originate from prompt decays of electroweak bosons are studied separately using a data-driven method similar to that of Ref. [60]. Their contributions are found to be negligible in all regions considered in this analysis. Finally, three regions are defined to validate the total background estimates with the data.

The selections used for the control and validation regions are summarised in Table 1 and illustrated in Figure 4. CR1 is defined as the envelope of SRA and SRB but requiring exactly one b-jet among the two leading jets. CR2 is also defined as the signal regions, but replacing the m_{T} requirements by 40–80 GeV.

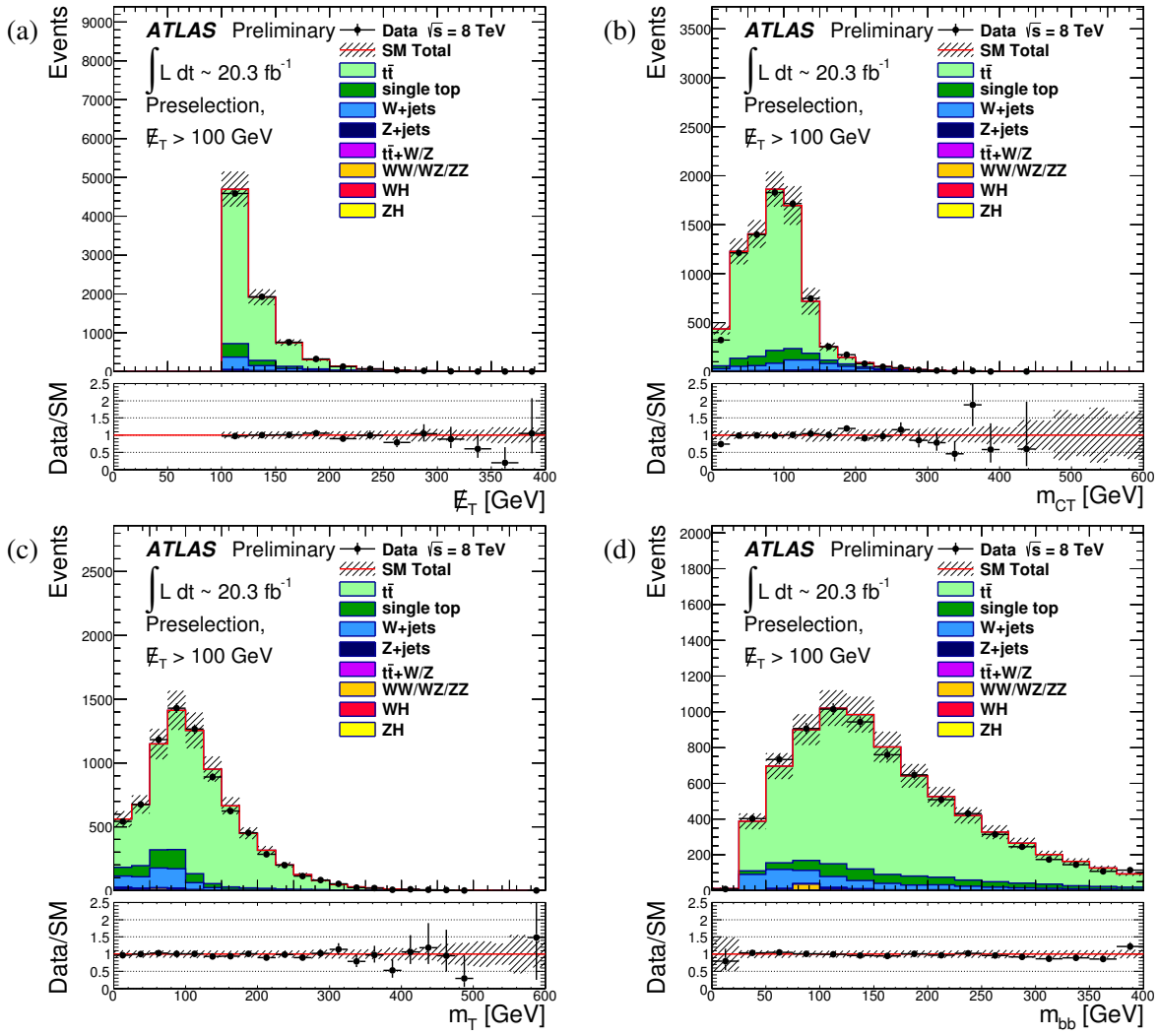

Figure 3: Distributions of (a) $E_{\mathrm{T}}^{\mathrm{miss}}$, (b) m_{CT}, (c) m_{T} and (d) m_{bb} for data and MC events passing the preselection. Also shown by the dotted and dashed lines are two representative signal models, added on top of the background predictions. The simulated backgrounds are normalized to the results from the background-only likelihood fit of the control regions (see Section 6 and 8). The ratio between observed and predicted event yields are also shown. The shaded bands around the expectations include statistical and systematic uncertainties. An $E_{\mathrm{T}}^{\mathrm{miss}}$ cut of 100 GeV is applied for all distributions.

The three validation regions are set as follows: VR0 is defined as CR1 but vetoing b-jets; VR1 and VR2 are defined as CR1 and CR2, respectively, but modifying the m_{T} requirements. In all regions, the invariant mass of the two leading jets (referred to as m_{jj}, m_{bj} and m_{bb} for 0, 1, 2 b-jets cases) is required

	SRA	SRB	CR1	CR2	VR0	VR1	VR2
Number of b-tagged jets	2	2	1	2	0	1	2
m_{T} (GeV)	100–130	> 130	> 100	40–80	> 100	40–100	80–100

Table 1: Definition of the signal, control and validation regions. All regions contain events with exactly one signal lepton, two or three signal jets, $m_{jj}/m_{bj}/m_{bb} > 50$ GeV, $E_{\mathrm{T}}^{\mathrm{miss}} > 100$ GeV and $m_{\mathrm{CT}} > 160$ GeV.

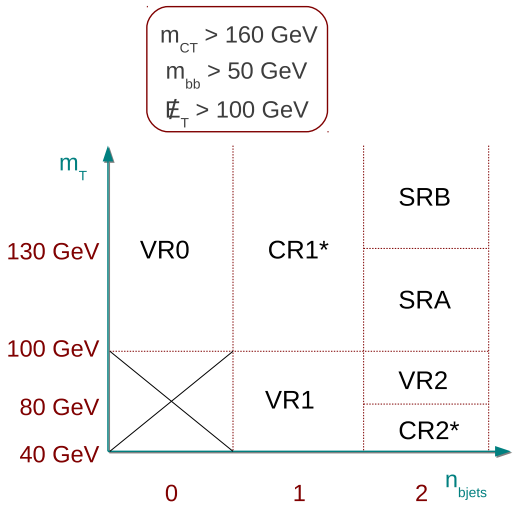

Figure 4: Control region (CR), validation region (VR) and signal region (SR) m_{T} and exclusive number of b-tagged jet selections. The asterisk (*) indicates that, in the background-only fit setup, only the m_{bb} sidebands are used to avoid the impact of potential signal contamination.

to be above 50 GeV. Both the control and validation regions are orthogonal to the signal regions.

The expected event composition of CR1 (CR2) is 47% (43%) $t\bar{t}$, 10% (15%) single top, 39% (36%) W + jets and 4% (6%) others. The W + jets composition in heavy-flavoured jets is 82% for CR1 and 97% for CR2.

The composition of VR0 is dominated (85%) by W + jets, with a large contribution from light-flavoured jets (72%). VR1 contains 53% W + jets (mostly from heavy-flavoured jets, 78%) and 40% $t\bar{t}$. Finally, VR2 is composed of 47% $t\bar{t}$, 33% W + jets (composed of 92% heavy-flavoured jets) and 14% single top.

7 Systematic Uncertainties

Statistical uncertainties arise from the limited number of simulated events. They are relevant only for the background samples in the signal regions.

Systematic uncertainties impact the estimates of the background and signal event yields in both the control and signal regions. The dominant experimental systematic uncertainties are due to the uncertainties on the jet energy scale calibration [61–66] and resolution [67], which are both also propagated to the $E_{\mathrm{T}}^{\mathrm{miss}}$ evaluation. An additional uncertainty on $E_{\mathrm{T}}^{\mathrm{miss}}$ is associated with soft energy deposits not assigned to any reconstructed objects. Experimental systematic uncertainties also include the lepton reconstruction, identification and trigger efficiencies, as well as lepton energy and momentum measurements [68–71]. The lepton energy scale uncertainties are also propagated to the $E_{\mathrm{T}}^{\mathrm{miss}}$ evaluation. Systematic uncertainties on the b-jet identification efficiency, and charm and light-flavour jet rejection factors [72] are also taken into account.

The uncertainty on the integrated luminosity is ±2.8%. It is derived from a preliminary calibration of the luminosity scale derived from beam-separation scans performed in November 2012 using the methodology detailed in Ref. [73],

Generator modelling uncertainties are obtained by comparing the predictions using the `POWHEG-BOX` and `MC@NLO` generators for top events, and the `POWHEG-BOX` and `SHERPA` generators for diboson events. Parton showering uncertainties are extracted in top events by comparing `POWHEG-BOX` plus `HERWIG` with

	SRA	SRB	CR1	CR2	VR0	VR1	VR2
Observed events	26	23	473	221	2440	4188	51
Fitted bkg events	24 ± 12	18 ± 6	480 ± 60	223 ± 33	2300 ± 600	4300 ± 600	68 ± 12
Fitted $t\bar{t}$ events	13 ± 12	8 ± 6	240 ± 90	110 ± 50	180 ± 100	1900 ± 800	36 ± 15
Fitted W + jets events	5.5 ± 2.3	2.9 ± 1.1	170 ± 60	68 ± 23	1900 ± 700	1900 ± 700	20 ± 7
Fitted single top events	4.8 ± 3.0	5.7 ± 2.9	50 ± 22	31 ± 15	38 ± 16	340 ± 120	9 ± 4
Fitted Z + jets events	$0.07^{+0.09}_{-0.07}$	0.34 ± 0.26	4.5 ± 2.5	0.33 ± 0.23	47 ± 24	18 ± 9	$0.11^{+0.12}_{-0.11}$
Fitted VV events	0.7 ± 0.5	1.2 ± 0.6	16^{+19}_{-16}	8.6 ± 1.5	110 ± 40	110 ± 80	2.2 ± 0.7
Fitted WH events	0.26 ± 0.15	0.19 ± 0.10	0.60 ± 0.33	3.6 ± 1.9	0.14 ± 0.09	5.8 ± 2.9	1.0 ± 0.5
Fitted ZH events	–	–	0.02 ± 0.01	0.02 ± 0.01	–	0.06 ± 0.03	0.01 ± 0.01
Fitted $t\bar{t}$+V events	0.15 ± 0.08	0.53 ± 0.28	2.7 ± 1.4	0.20 ± 0.11	2.0 ± 1.0	3.1 ± 1.6	0.12 ± 0.07
MC exp. SM events	23	18	510	220	2580	4380	70
MC exp. $t\bar{t}$ events	11	6	240	100	200	1700	33
MC exp. W + jets events	6.2	3.6	199	80	2190	2220	23.2
MC exp. single top events	4.7	7	49	33	41	350	10
MC exp. Z + jets events	0.07	0.33	4.5	0.34	46	17	0.11
MC exp. VV events	0.7	1.2	15	8.6	104	110	2.3
MC exp. WH events	0.27	0.19	0.60	3.7	0.13	5.7	1.0
MC exp. ZH events	0	0.01	0.02	0.02	0	0.06	0.01
MC exp. $t\bar{t}$+V events	0.15	0.53	2.7	0.20	1.9	3.1	0.12

Table 2: Event yields before and after background-only fit for the signal, control and validations regions. The uncertainties given are statistical plus systematic. Empty cells correspond to estimates lower than 0.01.

POWHEG-BOX plus PYTHIA. Special $t\bar{t}$ and single top samples are generated using ACERMC with PYTHIA to evaluate the uncertainties related to the amount of initial and final-state radiation. For single top, an additional uncertainty is assigned on the $t\bar{t}$ interference by using POWHEG-BOX samples using a different scheme to perform the diagram reduction. For smaller sources of background, namely Z+jets, $t\bar{t}$+V, W/Z+H, a conservative 50% theoretical uncertainty is assigned for all bins.

The main contributions to the systematic uncertainties in the background-only likelihood fit (see Section 8) originate from the jet energy scale with 9.0% (11.0%) and the b-tagging with 4.0% for both SRAh and SRBh on the experimental side, while the theoretical uncertainties are larger with 40% for SRAh and 20% for SRBh. The single top uncertainties constitute the largest contribution to the total theoretical uncertainties, with 27% (16%) for SRAh (SRBh).

8 Results

The results reported in the following sections are obtained using two different fit setups. In each setup, all regions are split into five m_{bb}[3] bins of 50–75, 75–105, 105–135, 135–165, and > 165 GeV.

In the first fit setup, the background in the signal region is estimated with a fit based on the profile likelihood method [74]. The inputs to the fit are as follows. For each channel:

1. the number of events observed in each of the control regions, and the corresponding number of events expected from simulation;

2. the transfer factors (obtained from the simulation) which relate the number of predicted W+jets or $t\bar{t}$ events in their associated control region to the one predicted in the signal region;

3. the number of events predicted by the simulation in each region for the Z+jets, diboson (VV), single top, W/Z+H and $t\bar{t}$+V backgrounds.

[3] m_{bb} is used here to designate $m_{jj}/m_{bj}/m_{bb}$ for the corresponding control and validation regions.

	SRAh	SRBh
Observed events	4	2
Background estimate		
$t\bar{t}$	2.9 ± 2.8	1.0 ± 0.6
W + jets	0.7 ± 0.4	0.3 ± 0.2
Single top	1.6 ± 1.3	0.6 ± 0.4
Z+jets	$0.01^{+0.02}_{-0.01}$	$0.00^{+0.01}_{-0.00}$
Diboson (VV)	$0.01^{+0.05}_{-0.01}$	$0.05^{+0.07}_{-0.05}$
WH	0.18 ± 0.10	0.12 ± 0.07
$t\bar{t}$+V	0.01 ± 0.01	0.11 ± 0.06
Total	5.4 ± 3.1	2.1 ± 0.7
Signal prediction		
(130, 0) GeV	6.5	0.2
(225, 0) GeV	1.9	4.1

Table 3: Observed and expected numbers of events in the signal region for the m_{bb} signal bin (SRAh and SRBh). The signal predictions are calculated with simplified models with different values of $(m_{\tilde{\chi}_1^\pm}, m_{\tilde{\chi}_1^0})$.

The number of events in each of these regions is described using a Poisson probability density function. There are two free parameters considered per channel: an overall normalization scale for the W+jets background and another one for the $t\bar{t}$ background. The other background sources are allowed to vary in the fit within their respective uncertainties. The statistical and systematic uncertainties (see Section 7) on the expected values are included in the fit as nuisance parameters which are typically constrained by Gaussian probability density functions with widths corresponding to the sizes of the uncertainties considered; correlations between regions and signal and background contributions are taken into account. The product of the various probability density functions forms the likelihood which the fit maximises by adjusting the free and nuisance parameters.

The background-only fit results are cross-checked in validation regions located around the control and the signal regions. The data in the validation regions are not used as constraints by the fits; they are only used to compare the results of the fit to statistically independent observations. The signal m_{bb} bin, 105–135 GeV, is excluded from the background-only fit to further reduce potential signal contamination in the control regions. The fit is then performed on a total of 8 exclusive bins.

Table 2 gives the results of the background-only fit to the control regions and of the extrapolation to the signal and validation regions. The small differences between the control regions fitted yields and observed events originate from the signal m_{bb} bin being excluded from the fit but not from the table. The predicted event yields in the validation and signal regions show good agreement with the observed data.

Figure 5 shows the m_{bj} distribution for CR1 and the m_{bb} distribution for CR2. Figure 6 shows the invariant mass distribution of the two leading jets for VR0, the two leading jets (one of which is a b-jet) for VR1, and the b-jet pair for VR2. The m_{bb} distributions in the signal regions are show in Figure 7. Good agreement is found within systematic uncertainties across the entire mass range for all regions. Table 3 show the observations and expectations for the SRAh and SRBh regions. Predictions by the simplified models are also shown in this region for different values of $(m_{\tilde{\chi}_1^\pm}, m_{\tilde{\chi}_2^0}, m_{\tilde{\chi}_1^0})$. The number of observed events in SRAh and SRBh are found in agreement with the SM expectations.

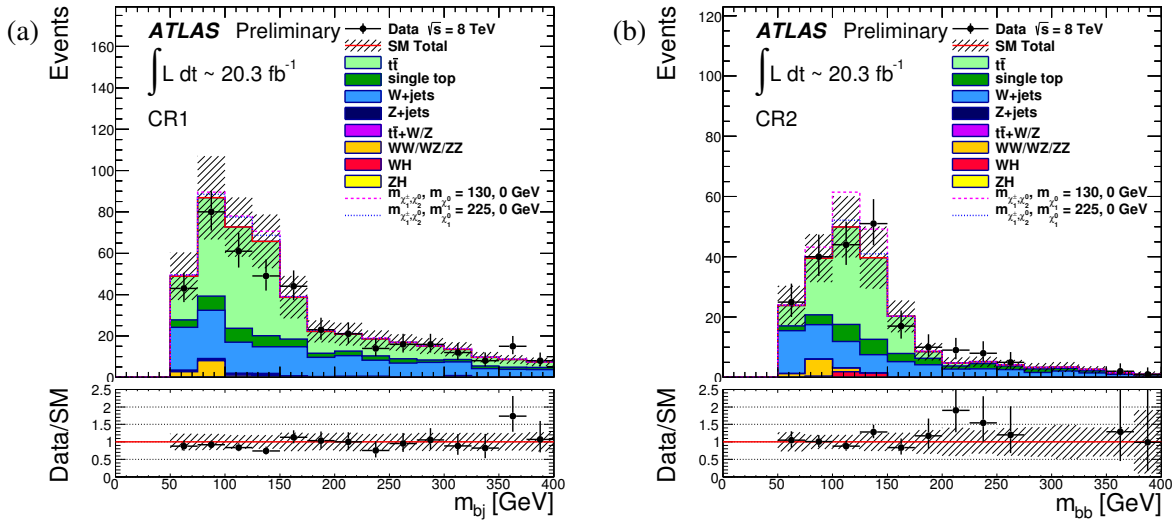

Figure 5: Distributions of m_{bj} and m_{bb}, respectively, for (a) CR1 and (b) CR2 for data and MC events. Also shown by the dotted and dashed lines are two representative signal models, added on top of the background predictions. The simulated backgrounds are normalized to the results from the background-only likelihood fit (see Section 8). The ratio between observed and predicted event yields are also shown. The shaded bands around the expectations include statistical and systematic uncertainties.

	SRAh	SRBh
Observed σ^{95}_{vis} (Asymptotic)	0.32 fb	0.21 fb
Observed S^{95}_{obs} (Asymptotic)	6.5	4.4
Expected S^{95}_{exp} (Asymptotic)	$7.0^{+3.1}_{-1.9}$	$4.4^{+2.5}_{-1.5}$
Observed σ^{95}_{vis} (Pseudo-experiments)	0.34 fb	0.21 fb
Observed S^{95}_{obs} (Pseudo-experiments)	6.9	4.4
Expected S^{95}_{exp} (Pseudo-experiments)	$7.0^{+2.8}_{-1.6}$	$4.4^{+1.8}_{-0.8}$

Table 4: Model-independent limits in the signal region for the m_{bb} signal bin (SRAh and SRBh). Shown are the observed 95% CL upper limits on the visible cross section, σ^{95}_{vis}, for non-SM events, and on the expected number of signal events, S^{95}_{exp} , for both the pseudo-experiment and asymptotic-formulae approaches.

9 Interpretation of the Results

In the absence of a significant excess over the SM background expectations, 95% confidence level (CL) exclusion limits are set.

Model-independent limits on the visible cross section, σ_{vis}, defined by the product of the production cross section, efficiency, and acceptance are derived from the number of observed and predicted events in each m_{bb} signal bin (SRAh and SRBh). The predicted events are extrapolated to the signal region from the background-only fit results. Limits on the number of non-SM events in the signal regions, derived using the CL_s prescription [75], are divided by the integrated luminosity to obtain the limits on the visible cross section. The limits at 95% CL are shown in Table 4. Results based both on pseudo-experiments and asymptotic formulae for a profile-log-likelihood test statistic [76] are given. The non-SM signal is assumed to contribute only to SRA and SRB in $105 < m_{bb} < 135$ GeV (SRAh and SRBh).

Limits can also be placed on specific models of physics beyond the SM. In this case, the fit is modified in the following way:

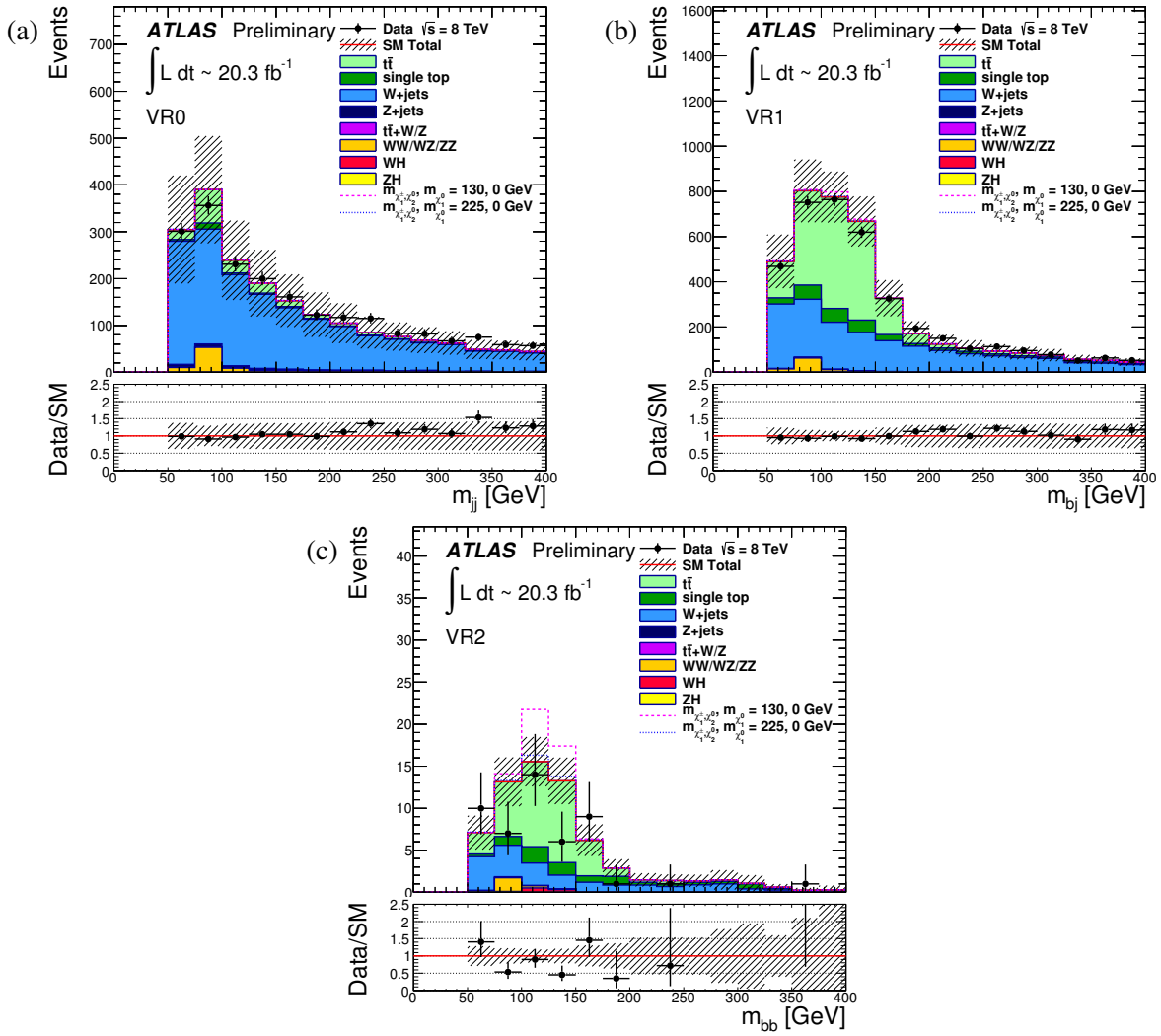

Figure 6: Distributions of m_{jj}, m_{bj} and m_{bb}, respectively for (a) VR0, (b) VR1 and (c) VR2 for data and MC events. Also shown by the dotted and dashed lines are two representative signal models, added on top of the background predictions. The simulated backgrounds are normalized to the results from the background-only likelihood fit (see Section 8). The ratio between observed and predicted event yields are also shown. The shaded bands around the expectations include statistical and systematic uncertainties.

1. there is an extra free parameter for a possible non-SM signal strength which is constrained to be non-negative;

2. the number of events observed in the signal regions, including the m_{bb} signal bin, is now also considered as an input to the fit. This amounts to 20 exclusive bins.

Furthermore, the expected contamination of the control regions by the signal is included in the fit. For example, the expected number of signal events in the signal m_{bb} bin of CR1 is 7.7 for the mass point $(m_{\tilde{\chi}_1^\pm}, m_{\tilde{\chi}_1^0})$=(130,0) and 6.1 for (225,0), and in the signal m_{bb} bin of CR2, the event yields for the same signal points are 17.4 and 4.1, respectively. Systematic uncertainties on the signal expectations stemming from detector effects are included in the fit in the same way as done for the backgrounds. Systematic uncertainties on the signal cross section due to the choice of renormalization and factorization scale and PDF uncertainties are calculated following the procedure described in [77].

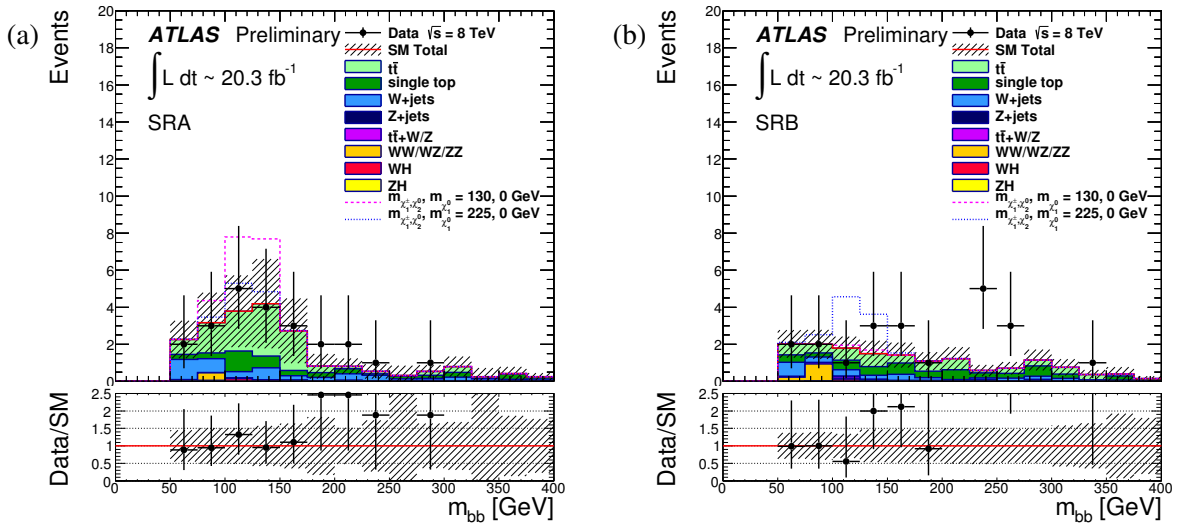

Figure 7: Distributions of m_{bb} for (a) SRA and (b) SRB for data and MC events. Also shown by the dotted and dashed lines are two representative signal models, added on top of the background predictions. The simulated backgrounds are normalized to the results from the background-only likelihood fit (see Section 8). The ratio between observed and predicted event yields are also shown. The shaded bands around the expectations include statistical and systematic uncertainties.

Figure 8 displays 95% CL exclusion region obtained in the $m_{\tilde{\chi}_1^0}$–$m_{\tilde{\chi}_1^\pm}$ plane. Shown are the expected (dashed blue) and observed (solid red) exclusion limits, including all uncertainties except the theoretical uncertainty on the signal cross section. The solid yellow band indicates the impact of experimental uncertainties on the expected limits whereas the dashed red lines around the observed limit show the changes in the observed limit as the signal cross sections are scaled up and down by the 1σ theoretical uncertainty. The expected exclusion limit at 68% CL is also drawn (dashed light blue). The combined signal expectation is relatively flat through large parts of the $m_{\tilde{\chi}_1^0}$–$m_{\tilde{\chi}_1^\pm}$ plane, and only slightly above (or around) the level of 95% CL exclusion (see Appendix B), making the analysis relatively sensitive to statistical fluctuations in the observed number of events, as indicated by the wide uncertainty band in Figure 8.

For values of $m_{\tilde{\chi}_1^0}$=0, the mass ranges of $125 < m_{\tilde{\chi}_1^\pm,\tilde{\chi}_2^0} < 141$ GeV and $166 < m_{\tilde{\chi}_1^\pm,\tilde{\chi}_2^0} < 287$ GeV are excluded at 95% CL, determined at -1σ signal theoretical uncertainty, with an expected exclusion range of $225 < m_{\tilde{\chi}_1^\pm,\tilde{\chi}_2^0} < 235$ GeV. Figures 9 shows the limits on the SUSY cross section as a function of $m_{\tilde{\chi}_1^\pm,\tilde{\chi}_2^0}$ for three different values of $m_{\tilde{\chi}_1^0}$.

10 Summary

A search for the production of chargino and neutralino decaying into final states with one charged lepton, missing transverse momentum, and two b-jets consistent with a Higgs boson has been performed. The proton–proton collision data used correspond to 20.3 fb^{-1} taken at $\sqrt{s} = 8$ TeV with the ATLAS detector at the LHC. No significant excess is observed with respect to the prediction from SM processes. Limits are set on the $\tilde{\chi}_1^\pm/\tilde{\chi}_2^0$ mass such that for massless $\tilde{\chi}_1^0$, the ranges $125 < m_{\tilde{\chi}_1^\pm,\tilde{\chi}_2^0} < 141$ GeV and $166 < m_{\tilde{\chi}_1^\pm,\tilde{\chi}_2^0} < 287$ GeV are excluded at 95% CL, determined at -1σ signal theoretical uncertainty, with an expected exclusion range of $225 < m_{\tilde{\chi}_1^\pm,\tilde{\chi}_2^0} < 235$ GeV.

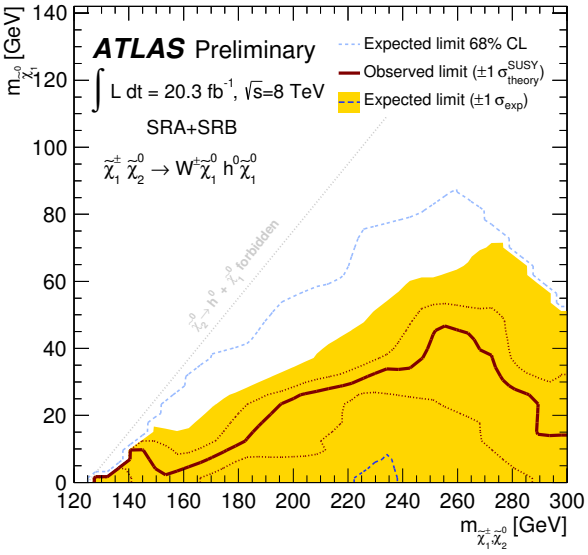

Figure 8: Exclusion limits in the $m_{\tilde{\chi}_1^\pm,\tilde{\chi}_2^0}$–$m_{\tilde{\chi}_1^0}$ plane. The dashed and solid lines show the 95% CL expected and observed limits, respectively, including all uncertainties except for the theoretical signal cross section uncertainty (PDF and scale). The solid band around the expected limit shows the $\pm 1\sigma$ result where all uncertainties are considered except those on the signal cross sections. The $\pm 1\sigma$ lines around the observed limit represent the results obtained when moving the nominal signal cross section up or down by the $\pm 1\sigma$ theoretical uncertainty. The 68% CL expected exclusion limit is also shown.

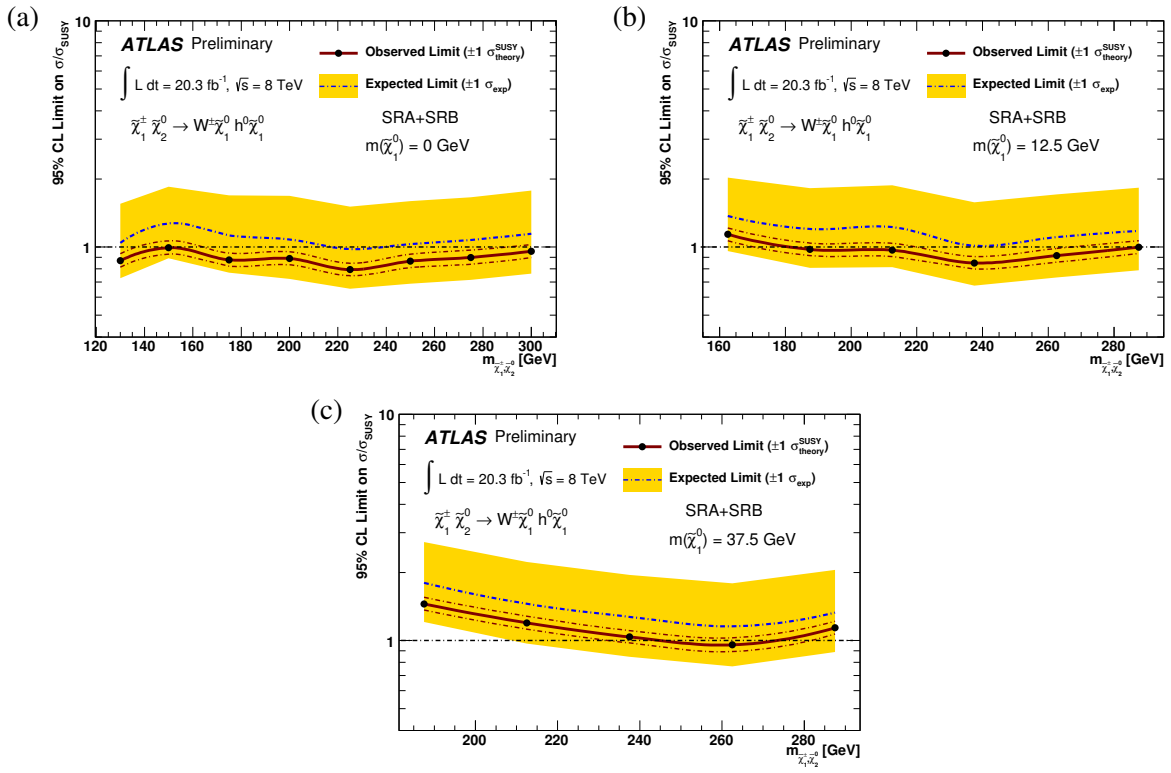

Figure 9: Exclusion limits as a function of $m_{\tilde{\chi}_1^\pm,\tilde{\chi}_2^0}$ for three values for $m_{\tilde{\chi}_1^0}$: (a) 0, (b) 12.5 GeV and (c) 37.5 GeV. The dashed and solid lines show the 95% CL expected and observed limits, respectively, including all uncertainties except for the theoretical signal cross section uncertainty (PDF and scale). The solid band around the expected limit shows the $\pm 1\sigma$ result where all uncertainties are considered except those on the signal cross sections. The $\pm 1\sigma$ lines around the observed limit represent the results obtained when moving the nominal signal cross section up or down by the $\pm 1\sigma$ theoretical uncertainty.

References

[1] H. Miyazawa, *Baryon Number Changing Currents*, Prog. Theor. Phys. **36 (6)** (1966) 1266–1276.

[2] P. Ramond, *Dual Theory for Free Fermions*, Phys. Rev. **D3** (1971) 2415–2418.

[3] Y. A. Gol'fand and E. P. Likhtman, *Extension of the Algebra of Poincare Group Generators and Violation of p Invariance*, JETP Lett. **13** (1971) 323–326. [Pisma Zh. Eksp. Teor. Fiz. **13** (1971) 452–455].

[4] A. Neveu and J. H. Schwarz, *Factorizable dual model of pions*, Nucl. Phys. **B31** (1971) 86–112.

[5] A. Neveu and J. H. Schwarz, *Quark Model of Dual Pions*, Phys. Rev. **D4** (1971) 1109–1111.

[6] J. Gervais and B. Sakita, *Field theory interpretation of supergauges in dual models*, Nucl. Phys. **B34** (1971) 632–639.

[7] D. V. Volkov and V. P. Akulov, *Is the Neutrino a Goldstone Particle?*, Phys. Lett. **B46** (1973) 109–110.

[8] J. Wess and B. Zumino, *A Lagrangian Model Invariant Under Supergauge Transformations*, Phys. Lett. **B49** (1974) 52.

[9] J. Wess and B. Zumino, *Supergauge Transformations in Four-Dimensions*, Nucl. Phys. **B70** (1974) 39–50.

[10] S. Weinberg, *Implications of Dynamical Symmetry Breaking*, Phys. Rev. **D13** (1976) 974–996.

[11] E. Gildener, *Gauge Symmetry Hierarchies*, Phys. Rev. **D14** (1976) 1667.

[12] S. Weinberg, *Implications of Dynamical Symmetry Breaking: An Addendum*, Phys. Rev. **D19** (1979) 1277–1280.

[13] L. Susskind, *Dynamics of Spontaneous Symmetry Breaking in the Weinberg- Salam Theory*, Phys. Rev. **D20** (1979) 2619–2625.

[14] P. Fayet, *Supersymmetry and Weak, Electromagnetic and Strong Interactions*, Phys. Lett. **B64** (1976) 159.

[15] P. Fayet, *Spontaneously Broken Supersymmetric Theories of Weak, Electromagnetic and Strong Interactions*, Phys. Lett. **B69** (1977) 489.

[16] G. R. Farrar and P. Fayet, *Phenomenology of the Production, Decay, and Detection of New Hadronic States Associated with Supersymmetry*, Phys. Lett. **B76** (1978) 575–579.

[17] P. Fayet, *Relations Between the Masses of the Superpartners of Leptons and Quarks, the Goldstino Couplings and the Neutral Currents*, Phys. Lett. **B84** (1979) 416.

[18] S. Dimopoulos and H. Georgi, *Softly Broken Supersymmetry and SU(5)*, Nucl. Phys. **B193** (1981) 150.

[19] R. Barbieri and G. F. Giudice, *Upper Bounds on Supersymmetric Particle Masses*, Nucl. Phys. **B306** (1988) 63.

[20] B. de Carlos and J. A. Casas, *One loop analysis of the electroweak breaking in supersymmetric models and the fine tuning problem*, Phys. Lett. **B309** (1993) 320–328, `arXiv:hep-ph/9303291`.

[21] The ATLAS Collaboration, *Search for the bb decay of the Standard Model Higgs boson in associated W/ZH production with the ATLAS detector*, Tech. Rep. ATLAS-CONF-2013-079, CERN, Geneva, Jul, 2013. http://cds.cern.ch/record/1563235.

[22] The ATLAS Collaboration, *Search for direct-slepton and direct-chargino production in final states with two opposite-sign leptons, missing transverse momentum and no jets in 20/fb of pp collisions at sqrt(s) = 8 TeV with the ATLAS detector*, Tech. Rep. ATLAS-CONF-2013-049, CERN, Geneva, May, 2013. http://cds.cern.ch/record/1547565.

[23] The ATLAS Collaboration, *Search for direct production of charginos and neutralinos in events with three leptons and missing transverse momentum in 21 fb^{-1} of pp collisions at $\sqrt{s} = 8$ TeV with the ATLAS detector*, Tech. Rep. ATLAS-CONF-2013-035, CERN, Geneva, Mar, 2013. http://cds.cern.ch/record/1532426.

[24] The ATLAS Collaboration, *Search for supersymmetry in events with four or more leptons in 21 fb^{-1} of pp collisions at $\sqrt{s} = 8$ TeV with the ATLAS detector*, Tech. Rep. ATLAS-CONF-2013-036, CERN, Geneva, Mar, 2013. http://cds.cern.ch/record/1532429.

[25] The CMS Collaboration, *Search for electroweak production of charginos, neutralinos, and sleptons using leptonic final states in pp collisions at 8 TeV*, Tech. Rep. CMS-PAS-SUS-13-006, CERN, Geneva, 2013. http://cds.cern.ch/record/1563142.

[26] The ATLAS Collaboration, *The ATLAS Experiment at the CERN Large Hadron Collider*, JINST **3** (2008) S08003.

[27] GEANT4 Collaboration, S. Agostinelli et al., *GEANT4: A simulation toolkit*, Nucl. Instrum. Meth. **A506** (2003) 250–303.

[28] W. Lukas, *Fast Simulation for ATLAS: Atlfast-II and ISF*, Journal of Physics: Conference Series **396** (2012) no. 2, 022031. http://stacks.iop.org/1742-6596/396/i=2/a=022031.

[29] The ATLAS Collaboration, *The ATLAS Simulation Infrastructure*, Eur. Phys. J. **C70** (2010) 823–874, arXiv:1005.4568 [physics.ins-det].

[30] S. Frixione, P. Nason, and C. Oleari, *Matching NLO QCD computations with Parton Shower similations: the POWHEG method*, JHEP **0711** (2007) 070.

[31] T. Sjostrand, S. Mrenna, and P. Skands, *PYTHIA 6.4 physics and manual*, JHEP **0605** (2006) 026, arXiv:hep-ph/0603175.

[32] S. Frixione and B. R. Webber, *Matching NLO QCD computations and parton shower simulations*, JHEP **0206** (2002) 029.

[33] S. Frixione, F. Stoeckli, P. Torrielli, B. R. Webber, and C. D. White, *The MC@NLO 4.0 Event Generator*, arXiv:1010.0819 [hep-ph].

[34] B. P. Kersevan and E. Richter-Was, *The Monte Carlo event generator AcerMC version 2.0 with interfaces to PYTHIA 6.2 and HERWIG 6.5*, arXiv:hep-ph/0405247.

[35] M. Cacciari, M. Czakon, M. Mangano, A. Mitov, and P. Nason, *Top-pair production at hadron colliders with next-to-next-to-leading logarithmic soft-gluon resummation*, Physics Letters B **710** (2012) no. 4–5, 612–622, arXiv:1111.5869 [hep-ph]. http://www.sciencedirect.com/science/article/pii/S0370269312002766.

[36] M. Aliev et al., *HATHOR: HAdronic Top and Heavy quarks crOss section calculatoR*, Comput. Phys. Commun. **182** (2011) 1034–1046, arXiv:1007.1327 [hep-ph].

[37] S. Frixione, E. Laenen, P. Motylinski, B. R. Webber, and C. D. White, *Single-top hadroproduction in association with a W boson*, JHEP **0807** (2008) 029, arXiv:0805.3067 [hep-ph].

[38] G. Corcella et al., *HERWIG 6: An event generator for hadron emission reactions with interfering gluons (including supersymmetric processes)*, JHEP **0101** (2001) 010, arXiv:hep-ph/0011363.

[39] J. Butterworth, J. Forshaw, and M. Seymour, *Multiparton interactions in photoproduction at HERA*, Z. Phys. **C72** (1996) 637–646, hep-ph/9601371.

[40] T. Gleisberg et al., *Event generation with SHERPA 1.1*, JHEP **0902** (2009) 007.

[41] M. L. Mangano, M. Moretti, F. Piccinini, R. Pittau, and A. D. Polosa, *ALPGEN, a generator for hard multiparton processes in hadronic collisions*, JHEP **0307** (2003) 001, arXiv:hep-ph/0206293.

[42] S. Catani, L. Cieri, G. Ferrera, D. de Florian, and M. Grazzini, *Vector Boson Production at Hadron Colliders: A Fully Exclusive QCD Calculation at Next-to-Next-to-Leading Order*, Phys. Rev. Lett. **103** (2009) 082001. http://link.aps.org/doi/10.1103/PhysRevLett.103.082001.

[43] S. Catani and M. Grazzini, *Next-to-Next-to-Leading-Order Subtraction Formalism in Hadron Collisions and its Application to Higgs-Boson Production at the Large Hadron Collider*, Phys. Rev. Lett. **98** (2007) 222002. http://link.aps.org/doi/10.1103/PhysRevLett.98.222002.

[44] A. Martin, W. Stirling, R. Thorne, and G. Watt, *Update of parton distributions at NNLO*, Physics Letters B **652** (2007) no. 5-6, 292 – 299. http://www.sciencedirect.com/science/article/pii/S0370269307008465.

[45] J. M. Campbell and R. K. Ellis, *An Update on vector boson pair production at hadron colliders*, Phys. Rev. **D60** (1999) 113006, arXiv:hep-ph/9905386.

[46] J. M. Campbell, R. K. Ellis, and C. Williams, *Vector boson pair production at the LHC*, JHEP **1107** (2011) 018, arXiv:1105.0020 [hep-ph].

[47] J. Alwall, M. Herquet, F. Maltoni, O. Mattelaer, and T. Stelzer, *MadGraph 5 : Going Beyond*, JHEP **1106** (2011) 128, arXiv:1106.0522 [hep-ph].

[48] J. M. Campbell and R. K. Ellis, *$t\bar{t}\,W^{\pm}$ production and decay at NLO*, JHEP **1207** (2012) 052, arXiv:1204.5678 [hep-ph].

[49] M. Garzelli, A. Kardos, C. Papadopoulos, and Z. Trocsanyi, *$t\bar{t}\,W^{\pm}$ and $t\bar{t}\,Z$ hadroproduction at NLO accuracy in QCD with parton shower and hadronization effects*, JHEP **1211** (2012) 056, arXiv:1208.2665 [hep-ph].

[50] S. Dittmaier et al., *Handbook of LHC Higgs Cross Sections: 1. Inclusive Observables*. CERN, Geneva, 2011. Comments: 153 pages, 43 figures, to be submitted to CERN Report. Working Group web page: https://twiki.cern.ch/twiki/bin/view/LHCPhysics/CrossSections.

[51] M. Bahr et al., *Herwig++ Physics and Manual*, Eur. Phys. J. **C58** (2008) 639–707, arXiv:0803.0883 [hep-ph].

[52] W. Beenakker, R. Hopker, M. Spira, and P. M. Zerwas, *Squark and gluino production at hadron colliders*, Nucl. Phys. **B492** (1997) 51–103, arXiv:hep-ph/9610490.

[53] The ATLAS Collaboration, *Measurement of the $W \to \ell\nu$ and $Z/\gamma^* \to \ell\ell$ production cross sections in proton-proton collisions at $\sqrt{s}$ = 7 TeV with the ATLAS detector*, JHEP **1012** (2010) 060, arXiv:1010.2130 [hep-ex].

[54] The ATLAS Collaboration, *Muon reconstruction efficiency in reprocessed 2010 LHC proton-proton collision data recorded with the ATLAS detector*, Tech. Rep. ATLAS-CONF-2011-063, CERN, Geneva, Apr, 2011. http://cds.cern.ch/record/1345743.

[55] M. Cacciari, G. P. Salam, and G. Soyez, *The anti-k_T jet clustering algorithm*, JHEP **0804** (2008) 063, arXiv:0802.1189 [hep-ph].

[56] The ATLAS Collaboration, *Jet energy measurement with the ATLAS detector in proton-proton collisions at $\sqrt{s}$ = 7 TeV*, Eur. Phys. J. **C73** (2013) 2304, arXiv:1112.6426 [hep-ex].

[57] The ATLAS Collaboration, *Commissioning of the ATLAS high-performance b-tagging algorithms in the 7 TeV collision data*, Tech. Rep. ATLAS-CONF-2011-102, CERN, Geneva, Jul, 2011. http://cds.cern.ch/record/1369219.

[58] D. Tovey, *On measuring the masses of pair-produced semi-invisibly decaying particles at hadron colliders*, JHEP **0804** (2008) 034.

[59] G. Polesello and D. Tovey, *Supersymmetric particle mass measurement with the boost-corrected contransverse mass*, JHEP **1003** (2010) 030.

[60] The ATLAS Collaboration, *Measurement of the top quark-pair production cross section with ATLAS in pp collisions at $\sqrt{s}$* = 7 TeV, Eur. Phys. J. **C71** (2011) 1577, arXiv:1012.1792 [hep-ex].

[61] The ATLAS Collaboration, *Jet energy measurement with the ATLAS detector in proton-proton collisions at $\sqrt{s}$ = 7 TeV*, Eur. Phys. J. **C73** (2013) 2304, arXiv:1112.6426 [hep-ex].

[62] The ATLAS Collaboration, *Jet energy scale and its systematic uncertainty in proton-proton collisions at $\sqrt{s}$ = 7 TeV with ATLAS 2011 data*, ATLAS-CONF-2013-004, http://cds.cern.ch/record/1509552.

[63] The ATLAS Collaboration, *In situ jet pseudorapidity intercalibration of the ATLAS detector using dijet events in $\sqrt{s}$ = 7 TeV proton-proton 2011 data*, ATLAS-CONF-2012-124, http://cds.cern.ch/record/1474490.

[64] The ATLAS Collaboration, *Pile-up corrections for jets from proton-proton collisions at $\sqrt{s}$ = 7 TeV in ATLAS in 2011*, ATLAS-CONF-2012-064, http://cds.cern.ch/record/1459529.

[65] The ATLAS Collaboration, *Probing the measurement of jet energies with the ATLAS detector using photon+jet events in proton-proton collisions at $\sqrt{s}$ = 7 TeV*, ATLAS-CONF-2012-063, http://cds.cern.ch/record/1459528.

[66] The ATLAS Collaboration, *Probing the measurement of jet energies with the ATLAS detector using Z+jet events from proton-proton collisions at $\sqrt{s}$ = 7 TeV*, ATLAS-CONF-2012-053, http://cds.cern.ch/record/1452641.

[67] The ATLAS Collaboration, *Jet energy resolution in proton-proton collisions at $\sqrt{s} = 7$ TeV recorded in 2010 with the ATLAS detector*, Eur. Phys. J. **C73** (2013) 2306, arXiv:1210.6210 [hep-ex].

[68] The ATLAS Collaboration, *Muon reconstruction efficiency in reprocessed 2010 LHC p-p collision data recorded with the ATLAS detector*, ATLAS-CONF-2011-063, http://cds.cern.ch/record/1345743.

[69] The ATLAS Collaboration, *A measurement of the muon reconstruction efficiency in 2010 ATLAS data using J/ψ decays*, ATLAS-CONF-2012-125, https://cds.cern.ch/record/1474642.

[70] The ATLAS Collaboration, *ATLAS Muon Momentum Resolution in the First Pass Reconstruction of the 2010 p-p Collision Data at $\sqrt{s} = 7$ TeV*, ATLAS-CONF-2011-046, http://cds.cern.ch/record/1338575.

[71] The ATLAS Collaboration, *Electron performance measurements with the ATLAS detector using the 2010 LHC proton-proton collision data*, Eur. Phys. J. **C72** (2012) 1909, arXiv:1110.3174 [hep-ex].

[72] The ATLAS Collaboration, *Measuring the b-tag efficiency in a $t\bar{t}$ sample with 4.7 fb^{-1} of data from the ATLAS detector*, ATLAS-CONF-2012-097, http://cds.cern.ch/record/1460443.

[73] The ATLAS Collaboration, *Improved luminosity determination in pp collisions at $\sqrt{s} = 7$ TeV using the ATLAS detector at the LHC*, Submitted to Eur. Phys. J **C** (2013) , arXiv:1302.4393 [hep-ex].

[74] G. Cowan, K. Cranmer, E. Gross, and O. Vitells, *Asymptotic formulae for likelihood-based tests of new physics*, Eur.Phys.J. **C71** (2011) 1554, arXiv:1007.1727 [physics.data-an].

[75] A. L. Read, *Presentation of search results: The CL_s technique*, J. Phys. **G28** (2002) 2693–2704.

[76] G. Cowan, K. Cranmer, E. Gross, and O. Vitells, *Asymptotic formulae for likelihood-based tests of new physics*, The European Physical Journal C **71** (2011) no. 2, 1–19. http://dx.doi.org/10.1140/epjc/s10052-011-1554-0.

[77] M. Kramer et al., *Supersymmetry production cross sections in pp collisions at $\sqrt{s} = 7$ TeV*, arXiv:1206.2892 [hep-ph].

A Cut flows for selected signal samples

Cut	Signal point (130,0) GeV	Signal point (225,0) GeV
Generated events	50000	50000
$E_{\mathrm{T}}^{\mathrm{miss}}$> 50 GeV	3256.49 ± 23.90	600.45 ± 3.73
≥2 central jets	2304.39 ± 20.12	458.03 ± 3.26
2 leading jets central	2170.64 ± 19.49	439.07 ± 3.19
Fourth-leading jet veto (p_{T}> 25 GeV)	1891.79 ± 18.20	369.43 ± 2.92
Additional baseline lepton veto	1860.44 ± 18.05	363.35 ± 2.89
m_{jj}> 50 GeV	1765.78 ± 17.57	345.63 ± 2.82
m_{T}> 40 GeV	1461.14 ± 15.99	305.45 ± 2.65
m_{CT}> 160 GeV	176.80 ± 5.60	52.48 ± 1.11
$E_{\mathrm{T}}^{\mathrm{miss}}$> 100 GeV	140.10 ± 4.99	45.48 ± 1.03
Exactly 2 leading b-tagged jets	45.62 ± 2.59	13.93 ± 0.53
SRA (100 GeV < m_{T} < 130 GeV)	8.72 ± 1.13	2.55 ± 0.23
SRB (m_{T} > 130 GeV)	0.35 ± 0.17	5.68 ± 0.33

Table 5: Number of simulated events entering the preselection for representative signal samples with ($m_{\tilde{\chi}_1^\pm}$,$m_{\tilde{\chi}_2^0}$,$m_{\tilde{\chi}_1^0}$) given by (130,0) and (225,0) GeV. The preselection consists of the event cleaning, single-lepton triggers, and the requirement of exactly one isolated electron or muon with p_{T} > 25 GeV. The events are weighted for differences in efficiencies between data and simulation as well as for cross section and the luminosity of 20.3 fb^{-1}.

B Additional figures

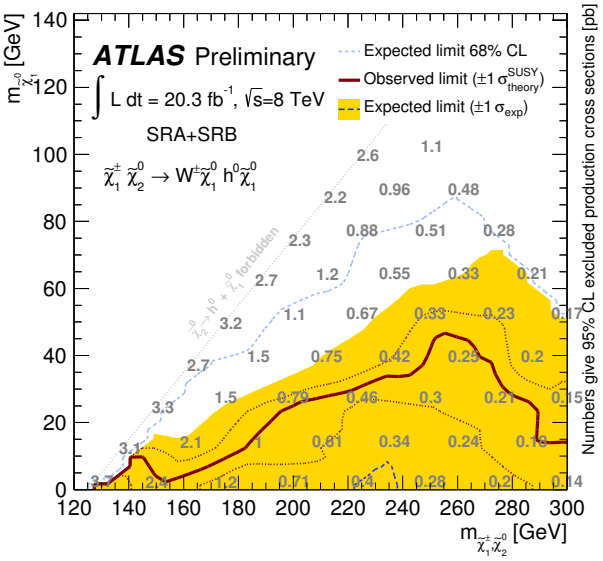

Figure 10: Exclusion limits in the $m_{\tilde{\chi}_1^\pm,\tilde{\chi}_2^0}$–$m_{\tilde{\chi}_1^0}$ plane. The dashed and solid lines show the 95% CL expected and observed limits, respectively, including all uncertainties except for the theoretical signal cross section uncertainty (PDF and scale). The solid band around the expected limit shows the $\pm1\sigma$ result where all uncertainties are considered except those on the signal cross sections. The $\pm1\sigma$ lines around the observed limit represent the results obtained when moving the nominal signal cross section up or down by the $\pm1\sigma$ theoretical uncertainty. The 68% CL expected exclusion limit is also shown. The 95% CL upper limits on the model-dependent production cross sections are given by the grey numbers.

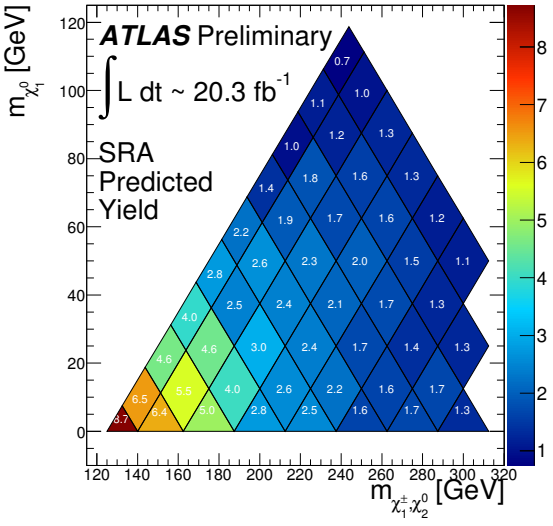

Figure 11: Predicted signal yields in the $m_{\tilde{\chi}_1^\pm,\tilde{\chi}_2^0}$–$m_{\tilde{\chi}_1^0}$ plane for SRA.

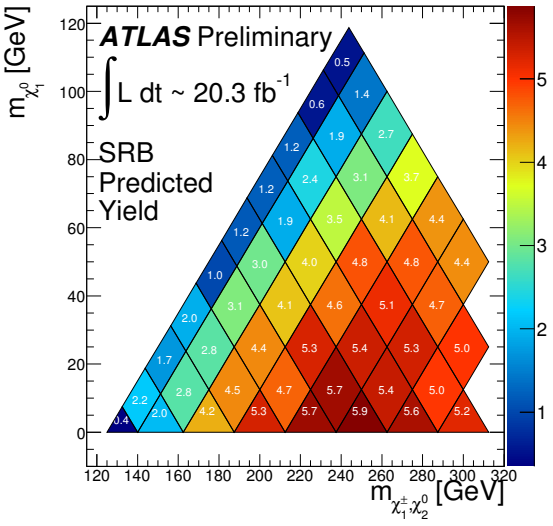

Figure 12: Predicted signal yields in the $m_{\tilde{\chi}_1^\pm,\tilde{\chi}_2^0}$–$m_{\tilde{\chi}_1^0}$ plane for SRB.